Ren *et al. Respiratory Research* (2025) 26:191
https://doi.org/10.1186/s12931-025-03278-7

Respiratory Research

RESEARCH Open Access

Transcription factor ZNF266 suppresses cancer progression by modulating CA9-mediated intracellular pH alteration in lung adenocarcinoma

Shencheng Ren[1†], Junkan Zhu[1†], Guangyao Shan[1†], Jiaqi Liang[1], Yunyi Bian[1], Han Lin[1], Haochun Shi[1], Binyang Pan[1], Guangyin Zhao[2], Huiqin Yang[1], Xiaolong Huang[1], Cheng Zhan[1*], Di Ge[1*] and Guoshu Bi[1*]

Abstract

Background Lung cancer remains the leading cause of cancer-related mortality globally, with lung adenocarcinoma (LUAD) being the most prevalent subtype. Despite extensive research efforts, the role of transcription factors in LUAD progression remains largely uncharacterized. In this study, we focused on ZNF266, a transcription factor whose impacts on LUAD have not been investigated.

Methods Using high-throughput sequencing data, we observed a significant downregulation of ZNF266 expression in LUAD tissues. To validate this finding, we conducted a retrospective analysis of nearly three thousand LUAD patients' data from public databases and our institution. Functional studies were performed using cell lines, organoids, and xenograft models to assess the role of ZNF266 in LUAD progression. RNA sequencing, chromatin immunoprecipitation, DNA pull-down assays, and dual-luciferase reporter assays were employed to elucidate the underlying mechanism. Additionally, adeno-associated virus (AAV)-mediated overexpression of ZNF266 was used to evaluate its therapeutic potential.

Results Patients with low ZNF266 expression had poorer prognosis compared to those with high expression. ZNF266 inhibits the malignant phenotypes of LUAD, including proliferation, migration, and invasion. Mechanistically, ZNF266 binds to the promoter region of CA9, suppressing its transcription. This leads to a reduction in intracellular pH and subsequent inhibition of the mTOR signaling pathway, which is crucial for cancer cell growth and survival.

†Shencheng Ren, Junkan Zhu, and Guangyao Shan contributed equally to this work.

*Correspondence:
Cheng Zhan
czhan10@fudan.edu.cn
Di Ge
ge.di@zs-hospital.sh.cn
Guoshu Bi
gsbi18@fudan.edu.cn

Full list of author information is available at the end of the article

Furthermore, AAV-mediated overexpression of ZNF266 significantly inhibited tumor growth in patient-derived xenograft models.

Conclusions Our study demonstrated that ZNF266 inhibits LUAD progression in a pH-dependent manner via modulating CA9 expression, uncovering its therapeutic significance for LUAD treatment.

Keywords Transcription factor, Lung adenocarcinoma, Intracellular pH, mTOR, Organoids

Background

Lung cancer remains one of the most frequently diagnosed malignancies and is the leading cause of cancer-related death globally [1]. Among its types, non-small cell lung cancer (NSCLC) accounts for approximately 85% of cases, with lung adenocarcinoma (LUAD) as the predominant subtype [2]. The primary treatment modalities for patients with LUAD encompass surgery, chemotherapy, radiation therapy, molecular targeted therapies, and immunotherapy [3]. Although great progress has been made in cancer treatment recently, the prognosis for LUAD patients remains poor, with a five-year survival rate under 26% [4].

Transcription factors (TFs) are proteins that recognize specific DNA sequences to control chromatin and transcription [5]. Aberrant expression of transcription factors leads to abnormal cell activities, including sustaining proliferative signaling, evading growth suppressors, and activating invasion and metastasis, which are also hallmarks of cancer [6]. Multiple agents targeting transcription factors, such as the MYC regulator RGT-61,159 [7] and the STAT3 inhibitor TTI-101 [8], have been assessed in clinical trials and exhibited promising efficacy in cancer treatment. Although thousands of transcription factors exist, the roles and therapeutic potential of many remain inadequately understood.

In this study, we demonstrated that Zinc Finger Protein 266 (ZNF266) potently inhibits the proliferation, migration, and invasion of LUAD both in vitro and in vivo. ZNF266 expression is significantly downregulated in LUAD, where it transcriptionally represses carbonic anhydrase IX (CA9), a pH regulator critical for maintaining cancer cell intracellular pH (pHi). This CA9–pHi axis activates the mammalian target of rapamycin (mTOR) signaling pathway, driving the malignant phenotypes of cancer. Most importantly, our findings from organoids and murine xenograft models confirmed the inhibitory role of ZNF266 in carcinogenesis. Notably, gene therapy utilizing peritumoral injection of adeno-associated virus (AAV) to deliver ZNF266 expression to the tumor significantly reduced the size of the xenograft tumors. Taken together, our study provides fundamental mechanistic insights into the role of ZNF266 and highlights its potential in the treatment of LUAD.

Methods

Bioinformatic analysis

Transcriptomic profiles alongside clinical and survival metadata for LUAD cases were retrieved from TCGA and GEO repositories. Employing the limma package (R/Bioconductor), differentially expressed genes (DEGs) were detected via an empirical Bayesian framework to model variance-stabilized expression shifts using moderated t-tests, with significance thresholds set at an adjusted $p < 0.001$ and absolute log2 fold change > 1.0. Survival outcomes were analyzed using Kaplan-Meier methodology through the survminer and survival R packages, supplemented by the Kaplan-Meier Plotter online resource (http://kmplot.com). The human transcription factor repertoire was obtained from the hTFtarget database. Publicly available ChIP-seq datasets were acquired from ENCODE and visualized using the Integrative Genomics Viewer (IGV). For functional annotation, DEGs derived from ZNF266-OE and negative control groups underwent pathway enrichment analysis via clusterProfiler, with Kyoto Encyclopedia of Genes and Genomes (KEGG) terms deemed significant at an adjusted $p < 0.05$ and false discovery rate (FDR) < 0.05.

Patients selection

Between February 2016 and October 2023, we gathered resected tumor tissue and corresponding clinical information from 173 patients with LUAD who underwent surgical resection at the Thoracic Surgery Department of Zhongshan Hospital, Fudan University. These procedures were performed by highly skilled thoracic surgeons, and the resected specimens, including tumors and lymph nodes, underwent thorough examination and confirmation by at least two competent pathologists. The staging of the tumors was determined according to the TNM classification system, as outlined in the eighth edition of the Cancer Staging Manual published by the American Joint Committee on Cancer (AJCC). This study strictly adhered to the ethical guidelines established in the Declaration of Helsinki and received approval from the Research Ethics Committee of Zhongshan Hospital, Fudan University (approval number: B2022-180R).

Cell lines and compounds

LUAD cell lines (A549 and PC-9) were sourced from the Chinese Academy of Sciences cell bank. Short Tandem

Repeat (STR) profiling confirmed the genetic identity and purity of these lines, with cells under 30 passages used for experimental work. Cells were cultured in DMEM high-glucose medium (KeyGEN BioTECH, Nanjing, China), enriched with either 10% fetal bovine serum (Lonsera, Shuangru Biotechnology Co., Ltd, Suzhou, China) or dialyzed fetal bovine serum (VivaCell, Shanghai, China), along with 0.1 mg/ml streptomycin and 100 U/ml penicillin (Beyotime, Shanghai, China). Culturing was conducted in a 37 °C incubator under a 5% CO_2, humidified environment. Sodium hydroxide (NaOH in PBS) and hydrochloric acid (HCl, 37 wt % in water) were purchased from Aladdin (Shanghai, China).

Lentiviral infections and CRISPR/Cas9-mediated gene knockout

Lentiviral vectors for ZNF266, CA9, and negative control were developed by Genechem Technology (Shanghai, China). Cells were transfected with these lentiviruses using HiTrans A reagent (Genechem Technology) as per the manufacturer's instructions and then selected with puromycin (Beyotime) for 48 h. To achieve precise gene knockout, CRISPR/Cas9 technology was employed in the cell lines. Specific sgRNAs targeting ZNF266 were designed and incorporated into GV392 plasmids, which included both puromycin resistance and the hSpCas9 gene. To achieve the overexpression of ZNF266 after knockout, the vectors carrying modified ZNF266 cDNA sequence refractory to the inhibition of sgRNAs were generated. These modified vectors were subsequently packaged into lentiviruses within HEK-293T cells. Genechem Technology conducted the entire process of vector design, assembly, and lentivirus packaging. Table S3 provides further details on the sgRNA used.

RNA sequencing

To investigate the transcriptional response of ZNF266 overexpression in A549, total RNA was extracted using the TRIzol reagent (TIANGEN, Beijing, China). Sequencing was conducted by OE Technology (Shanghai, China), and the raw data were normalized to Fragments Per Kilobase of exon model per Million mapped fragments (FPKM) format for subsequent analysis.

RNA isolation and quantitative real-time PCR (qRT-PCR)

RNA extraction was carried out using TRIzol reagent sourced from TIANGEN. Following this, the isolated RNA was converted into cDNA employing the Hifair II First-Strand cDNA Synthesis Kit, manufactured by YEASEN (Shanghai, China). The qRT-PCR reactions were conducted using Hieff qPCR SYBR Green Master Mix (YEASEN) on an ABI QuantStudio 5 real-time PCR platform provided by Thermo Fisher Scientific. Each experimental sample was assayed in triplicate, and the relative mRNA expression levels were calculated using the 2-ΔΔCT method. For normalization, β-actin was used as an endogenous reference gene. The primers used in this study are listed in Table S4.

Western blot

Cell lysates were generated by homogenizing samples in ice-cold RIPA buffer (Beyotime) containing a protease inhibitor cocktail and two phosphatase inhibitors (TargetMol). Protein levels were quantified via the BCA assay (YEASEN) according to the manufacturer's protocol. For immunoblotting, 20 μg of protein per sample was resolved on SDS-PAGE gels and electrophoretically transferred to PVDF membranes (Millipore). Membranes were blocked for 1 h at room temperature with 5% non-fat milk dissolved in Tris-buffered saline containing 0.1% Tween-20 (TBST). Primary antibody incubations were performed overnight at 4 °C, followed by three 10-min TBST washes to remove unbound antibodies. Horseradish peroxidase (HRP)-linked secondary antibodies (Beyotime; 1:2,500 dilution) were applied for 1 h at room temperature. Chemiluminescent signals were captured using BeyoECL Moon substrate (Beyotime), with exposure times optimized for band clarity. β-actin was uniformly employed as the normalization control across all experimental conditions. A full list of primary antibodies, including dilutions and vendors, is provided in Table S5.

Cell viability assay

To assess cell proliferation, cells were plated in quintuplicate into 96-well plates at a density of 1,500 cells per well during their logarithmic growth phase. Then the cell viability was measured as previously described [9]. Following incubation at 37 °C for various durations (0, 24, 48, 72, 96, and 120 h), cell proliferation was evaluated using the Enhanced Cell Counting Kit-8 Viability Assay Kit (Topscience, Shanghai, China), adhering strictly to the manufacturer's instructions.

High-content imaging system analysis

For the analysis utilizing the high-content imaging system, cells transfected with lentivirus carrying the Green Fluorescent Protein (GFP) sequence were seeded in quintuplicate into 96-well plates at a density of 1,800 cells per well during the logarithmic growth phase. Subsequently, the plates were positioned within the Operetta CLS High-Content Analysis System (PerkinElmer, Waltham, USA), which was set to a 37 °C incubator with 5% CO_2 and maintained under these conditions for 120 h. Meanwhile, the fluorescence images of the cells were captured and analyzed at 24-hour intervals using the Harmony 4.9 software.

Wound healing assay

On average, various cell groups were seeded into a 6-well plate. These cells were allowed to proliferate into a monolayer and subsequently scratched manually using a 200 μL pipette tip. The cells were then rinsed with phosphate-buffered saline (PBS) and incubated at 37 °C in media devoid of serum. Phase-contrast microscopy was used to capture images of the wounded areas at 24-hour intervals. Each experiment was independently replicated three times to ensure reproducibility.

Transwell migration and invasion assay

The abilities of cell migration and invasion were assessed using Transwell assays as previously described [10]. Specifically, LUAD cells (3×10^4 cells/well) were plated in the upper chamber (BIOFIL, Guangzhou, China), either without (for the Transwell migration assay) or with (for the Transwell invasion assay) Matrigel coating (YEASEN), following the manufacturer's instructions. Subsequently, serum-free medium was added to the upper chambers, while the lower chambers contained serum-rich medium. The cells were then incubated for 24 h at 37 °C, in an atmosphere of 5% CO_2. After incubation, the cells that had migrated or invaded into the lower chambers were fixed with 4% paraformaldehyde for 10 min and stained with 0.5% crystal violet. Images of each assay were captured using an inverted microscope (Olympus, Tokyo, Japan), and the cell counts within each chamber were determined using ImageJ software. The experiments were conducted in triplicate to ensure reproducibility.

Intracellular pH (pHi) detection in vitro

There are three methods for detecting pHi in vitro using BCECF (20,70-bis-(2-carboxyethyl)-5(and-6)-carboxyfluorescein)-AM probes (Dojindo, Kumamoto, Japan). In the first method, cells from various groups were seeded in 24-well plates. Following 24 h of incubation, cells were treated in PBS solution containing 2 μM BCECF-AM at 37 °C for 20 min. Fluorescence was then measured using an inverted microscope (Olympus) with excitation at 488 nm. In the second method, cells from various groups were seeded in 24-well plates and incubated for 24 h. They were subsequently treated in PBS solution containing 2 μM BCECF-AM at 37 °C for 20 min, then trypsinized, washed, and resuspended in 0.5 mL of PBS for flow cytometry analysis. At least 20,000 cells were analyzed per condition using FlowJo software (TreeStar, Woodburn, OR, USA). In the third method, as previously described [11, 12], cells were seeded in 96-well plates. Upon reaching 60–70% confluency, cells were treated with 2 μM BCECF-AM in phosphate-buffered saline (PBS) for 20 min at 37 °C. Fluorescent signals were quantified using a microplate reader, with dual excitation wavelengths (440 nm and 490 nm) and emission at 530 nm. For pH calibration, cells labeled with BCECF-AM were equilibrated for 10 min in high-potassium buffers adjusted to predefined pH ranges (6.2–6.6, 7.0–7.4, 7.8) containing 10 μM nigericin, a K+/H + ionophore, prior to signal acquisition.

Chromatin Immunoprecipitation (ChIP) assay

The ChIP assays were conducted using the SimpleChIP® Plus Enzymatic Chromatin IP Kit (Magnetic Beads) (CST, Danvers, USA) as previously described [13]. Chromatin fragmentation was initiated by formaldehyde cross-linking of intact cells, followed by membrane disruption and digestion with micrococcal nuclease (MNase). Following fragmentation, previously cross-linked chromatin was subjected to immunoprecipitation using monoclonal antibodies specific to the target proteins, with incubations performed overnight at 4 °C. For positive and negative controls, a Histone H3 antibody (CST) and human IgG (CST) were used, respectively. The specific antibodies used are listed in Table S5. Following extensive washing, DNA was eluted from the beads and subjected to qPCR analysis.

DNA pull-down assay

For DNA pull-down assays, 5'-biotinylated primers were employed to generate oligonucleotide probes by PCR amplification. Probe integrity was confirmed by 1.5% agarose gel electrophoresis, followed by purification with a commercial gel extraction kit (TaKaRa). Streptavidin-coated magnetic beads (CST) were conjugated with 1 mg biotinylated DNA probes in 20 mL binding buffer. After magnetic capture and three washes with ice-cold BS/THES buffer, beads were incubated with 250 μg nuclear extracts. Negative controls utilized unmodified beads, while competition assays included 20 μg unlabeled probe. Rotational incubation at 4 °C for 12 h included 100 μg/mL salmon sperm DNA (Solarbio) and 10 μg/mL BSA to block nonspecific interactions. Protein-DNA complexes were eluted with SDS sample buffer prior to immunoblotting.

Dual-luciferase reporter assay

The predicted target sites' CA9 promoter sequence and its corresponding mutated variant were cloned into firefly luciferase reporter plasmid vectors by Genechem. Subsequently, these plasmids were transfected into either control or ZNF266-overexpressing 293T cells utilizing the lipo8000 transfection reagent supplied by Beyotime. Additionally, renilla luciferase reporter plasmids were co-transfected during this process. 48 h post-transfection, dual-luciferase reporter assays were conducted using the Beyotime Luciferase Reporter Gene Assay Kit.

Establishment of patient-derived organoids (PDOs) and viability assay

LUAD tumor tissues were utilized to establish PDOs. The experimental procedures were performed as previously described [11, 14]. Initially, the tissues were meticulously dissected into smaller fragments and thoroughly rinsed three times with ice-cold Hank's Balanced Salt Solution (HBSS), enriched with 0.3 mg/mL streptomycin and 300 units/mL penicillin. Enzymatic digestion was then performed using a specialized organoid digestive solution sourced from D1Med (Shanghai, China). Following filtration and centrifugation steps, the resultant cell precipitate was resuspended in a 25-fold excess of Matrigel (YEASEN) and plated into a 24-well dish. After allowing the Matrigel to solidify at 37 °C for 25 min, each well received 500 μL of human LUAD-PDO culture medium (D1Med) to support PDO growth.

For lentiviral transfection, PDOs were dissociated into individual cells by a specialized organoid digestive solution (Absin, Shanghai, China) and resuspended in 500 μL of human LUAD-PDO culture medium. Transfection was achieved using HiTrans A reagent, adhering to the manufacturer's guidelines, for 24 h. Subsequently, the cells were harvested, resuspended in a 25-fold volume of Matrigel, and subjected to puromycin selection for 72 h.

For histological examination, PDOs were collected and fixed in 4% paraformaldehyde. They were then embedded in a combination of agarose and paraffin, sectioned, and processed through standard hematoxylin and eosin staining protocols, which included deparaffinization, dehydration, and staining steps.

To evaluate the viability of PDOs across different groups, they were plated in 96-well plates. Cell viability assessments were conducted using the CellTiter-Lumi Luminescent 3D Cell Viability Assay Kit (Beyotime).

Xenograft studies

The study adhered to the ethical standards set by the Research Ethics Committee at Zhongshan Hospital, affiliated with Fudan University. To establish cell-derived tumor xenograft models (CDXs), 1×10^6 A549 cells from various groups were injected subcutaneously into the right flanks of 4-week-old male BALB/c nude mice, sourced from GemPharmatech (Nanjing, China), using 100 μL of PBS as the carrier. Tumor growth was assessed every 3 days with vernier calipers, starting 10 days post-tumor formation. After 4 weeks, the mice were euthanized, and tumor volumes were calculated employing the formula: (length × width^2) / 2. To ensure objectivity, the researchers were blinded to the group allocations during the outcome evaluations.

For the development of patient-derived tumor xenograft models (PDXs), freshly resected tumor specimens from two patients with LUAD were collected and utilized. These samples were transplanted onto the backs of 4-week-old male NSG mice to generate two PDX models (PDX-1 and PDX-2). Before transplantation, the surgical tumor tissues were washed with a 10× solution of penicillin-streptomycin and subsequently cut into 2-mm^3 fragments in PBS containing penicillin-streptomycin. The tumor fragments were mixed with Ceturegel Matrix (YEASEN) and PBS in a 1:1 ratio before implantation (P0). Once the graft tumors reached a volume of 200 mm^3, they were excised, dissected into smaller pieces, and passaged to another set of NSG mice (P1). Subsequently, P2 PDX models were established. Tumor volumes were measured biweekly by determining the length and width using calipers and applying the formula: (length × width^2) / 2. The safety profile of AAV-ZNF266 was rigorously evaluated through monitoring of hematological indices, serum biochemistry, and body weight in mice over a 28-day period. These assessments were conducted relative to peritumorally administered PBS controls to isolate vector-specific effects. In the treatment studies, AAV-Vector (1×10^{10} vg/mL) and AAV-ZNF266 (1×10^{10} vg/mL) were injected peritumorally into the mice bearing PDXs. AAV expressing human ZNF266 was produced and purchased from Genechem.

Immunohistochemical (IHC) staining

Tissue samples from patients with LUAD were formalin-fixed and paraffin-embedded. The slides underwent a baking process at 65 °C for a duration of overnight, followed by three consecutive dewaxing procedures in xylene, each lasting 15 min. Rehydration was accomplished through a series of graded ethanol immersions. Antigen retrieval was carried out using citrate buffer sourced from Sangon Biotech (Shanghai, China), and the slides were then treated with peroxidase blocking buffer at 37 °C for 30 min to reduce non-specific binding interactions. Following a 10-minute incubation in blocking buffer, the slides were incubated with primary antibodies at 4 °C overnight, with a subsequent incubation with a secondary antibody for 30 min at room temperature. The staining process was executed utilizing the GTVisionTM III Detection System/Mo&Rb (GeneTech, Shanghai, China), adhering to the manufacturer's guidelines. The primary antibodies employed for IHC staining are detailed in Table S5.

For the quantitative assessment of IHC staining, the evaluation criteria encompassed both staining intensity and the proportion of positively stained cells. The immunoreactivity score (IRS) was calculated as follows: IRS = Staining intensity × Proportion of positive-stained cells. The staining intensity of the colored cells was graded as follows: 0 (absent/negative), 1 (light yellow/weak), 2 (brownish-yellow/moderate), and 3 (brown/strong).

Multiplex immunohistochemistry (mIHC)

Each tissue section underwent the IHC processing steps outlined previously, including paraffin removal, dewaxing with xylene, rehydration, antigen retrieval, temperature reduction, permeabilization, and blocking procedures. Following this, the sections were incubated with primary antibodies at 4 °C overnight, with subsequent washing in PBS to eliminate unbound antibodies. Thereafter, the sections were incubated with their respective secondary antibodies for one hour and then treated with Tyramide signal amplification (TSA) reagents sourced from Servicebio (Wuhan, China) for 10 min at room temperature. To strip the tissue-bound primary and secondary antibodies, the sections were immersed in a citrate repair solution (pH 6.0) and heated in a microwave oven to maintain boiling for 10 min. This blocking step was repeated, followed by a second application of primary antibodies, subsequent incubation with secondary antibodies, and another treatment with TSA reagents. For nuclear staining, the slides were counterstained with DAPI (Servicebio). The TSA reagents used were as follows: iF440-Tyramide (dilution 1:500), iF488-Tyramide (dilution 1:500), iF546-Tyramide (dilution 1:500), and iF647-Tyramide (dilution 1:500). The primary antibodies utilized in each staining protocol are detailed in Table S5.

Data presentation and statistical analysis

Each experiment was independently replicated a minimum of three times, and the outcomes were presented as the mean with its corresponding standard deviation. Statistical computations and graphical representations were performed using R software, version 4.4.0 (R Foundation for Statistical Computing, Vienna, Austria), ImageJ (National Institutes of Health, USA), IBM SPSS Statistics 20 (USA) and GraphPad Prism 10 (GraphPad Software, La Jolla, California, USA). Depending on the nature of the continuous variables, either an unpaired Student's t-test or one-way or two-way ANOVA was employed to ascertain statistical differences. All tests were two-tailed, and statistical significance was established at a p-value threshold of less than 0.05.

Results

ZNF266 is decreased in LUAD and associated with poor prognosis

To identify TFs that may play a crucial role in the progression of LUAD, we analyzed data from The Cancer Genome Atlas Program (TCGA) and The Genotype-Tissue Expression (GTEx) databases. By overlapping the sets of human genes that were both differentially expressed in LUAD and associated with prognosis, we uncovered three significant genes: ZNF266, ZEB2, and ZNF493 (Fig. 1A). The effects and mechanisms of ZEB2 have been extensively studied in previous research [15, 16]. Meanwhile, the fold change of ZNF266, as well as its hazard ratio (HR) concerning survival, was more significant than ZNF493. Given the significance of the observed differences and the gaps in current research, we chose ZNF266 as the focus of our study.

We first investigated the clinical implications of ZNF266 in LUAD patients. RNA sequencing (RNA-seq) data from the TCGA and the GTEx databases, including both unpaired samples (normal group = 347, tumor group = 513) and paired samples (n = 58), revealed that the expression of ZNF266 was significantly downregulated in LUAD (Fig. 1B and C). Moreover, low expression of ZNF266 in LUAD patients indicated a poorer prognosis, as demonstrated by the Kaplan–Meier plotter database analysis, the TCGA database analysis and the GEO database analysis (Fig. 1D and E, S1A and S1B). Then, we obtained samples from LUAD patients who underwent radical surgery at Zhongshan Hospital Fudan University between February 2016 and October 2023. The quantitative real-time PCR (qRT-PCR), Western blot, and immunohistochemistry (IHC) analysis confirmed the downregulation of ZNF266 in LUAD tissue (Fig. 1F-I). According to the staining intensity of ZNF266 in IHC, 142 patients (clinicopathological characteristics summarized in Table S1) were divided into low-ZNF266 (n = 80) and high-ZNF266 (n = 62) groups. Notably, the low-ZNF266 group exhibited a higher T stage and N stage compared to the high-ZNF266 group. Kaplan-Meier survival analysis also demonstrated that the low-ZNF266 group had significantly shorter overall survival (OS) compared to the high-ZNF266 group (Fig. 1J). Furthermore, univariate and multivariate Cox regression analyses identified high ZNF266 expression as a significant and independent predictor of better OS for LUAD patients (Table S2). Based on the Cox regression analysis, a nomogram was constructed that incorporated the predictors of OS, including age, pathologic T stage, pathologic N stage, pathologic M stage, and ZNF266 (Fig. 1K). The calibration curves demonstrated good reproducibility and predictability of the nomogram model during internal validation (Fig. 1L). Taken together, the above results indicate that the transcription factor ZNF266 is downregulated and serves as a prognostic biomarker for LUAD.

ZNF266 inhibits the proliferation, migration, and invasion of LUAD

To explore the function of ZNF266 in LUAD, we first generated ZNF266-knockout (KO) and ZNF266-over-expressing-after-knockout (OE) LUAD cell lines (A549 and PC-9) using lentiviral vectors (Fig. 2A and S2A). CCK8 assays and high-content imaging analysis demonstrated that in comparison to the negative control (NC) cells, ZNF266-KO resulted in a significant increase in

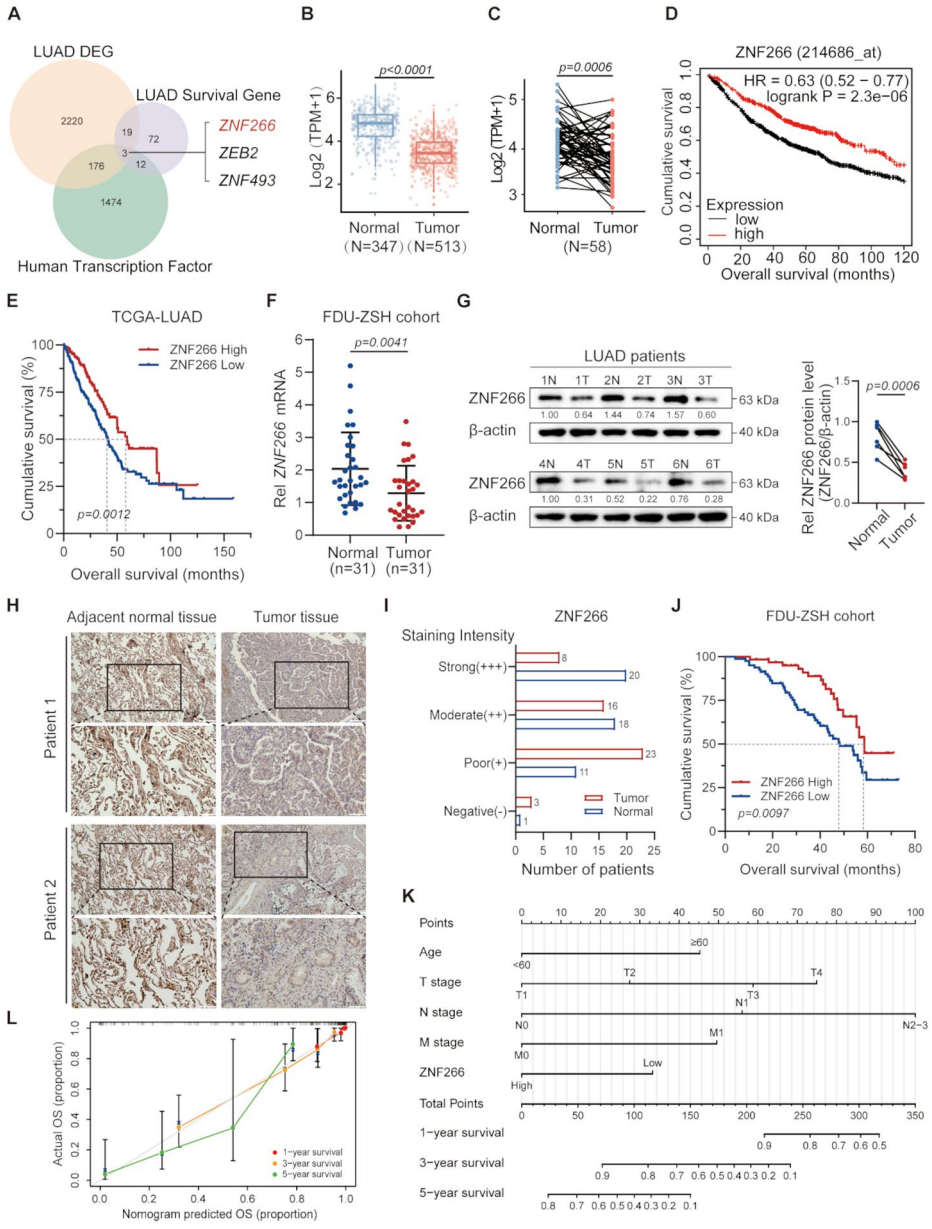

Fig. 1 ZNF266 is decreased in lung adenocarcinoma (LUAD) and associated with poor prognosis. **(A)** Venn diagram demonstrates the sets of genes that were differentially expressed in LUAD, those associated with prognosis, and human transcription factors. **(B-C)** ZNF266 expression levels in normal and tumor samples from the TCGA-LUAD and GTEx databases, including both unpaired samples (normal group = 347, tumor group = 513) **(B)** and paired samples ($n = 58$) **(C)**. **(D-E)** Kaplan–Meier analysis of overall survival comparing the high and low expression of ZNF266 in LUAD patients in the Kaplan–Meier plotter database **(D)** and the TCGA database **(E)**. **(F)** RT-qPCR analysis of ZNF266 mRNA expression in 31 LUAD tumor tissues and paired normal tissues from Fudan University-affiliated Zhongshan Hospital cohort (FDU-ZSH cohort). **(G)** Western blot analysis of ZNF266 protein expression in paired LUAD tissues. **(H-I)** Representative images **(H)** and quantification **(I)** of immunohistochemistry (IHC) staining of ZNF266 in LUAD tissues and paired normal tissues. Scale bars, 200–100 μm. **(J)** Kaplan–Meier analysis of overall survival according to ZNF266 expression in LUAD patient samples from the FDU-ZSH cohort. **(K)** Nomogram plot predicting the overall survival probability. **(L)** Calibration curve of the nomogram using the bootstrap method in internal validation. Error bars validated the standard error of the mean within the current data set

proliferation (Fig. 2B and C). Conversely, ZNF266-OE cells exhibited a decreased proliferation rate (Fig. 2B and C). Wound healing and transwell assays revealed that knockout of ZNF266 enhanced the migration and invasion of LUAD cells, whereas overexpression of ZNF266 exhibited opposite results (Fig. 2D and E).

Furthermore, we successfully established patient-derived organoids (PDOs) and created ZNF266-KO, OE, and NC PDO models (Fig. 2F). The histological

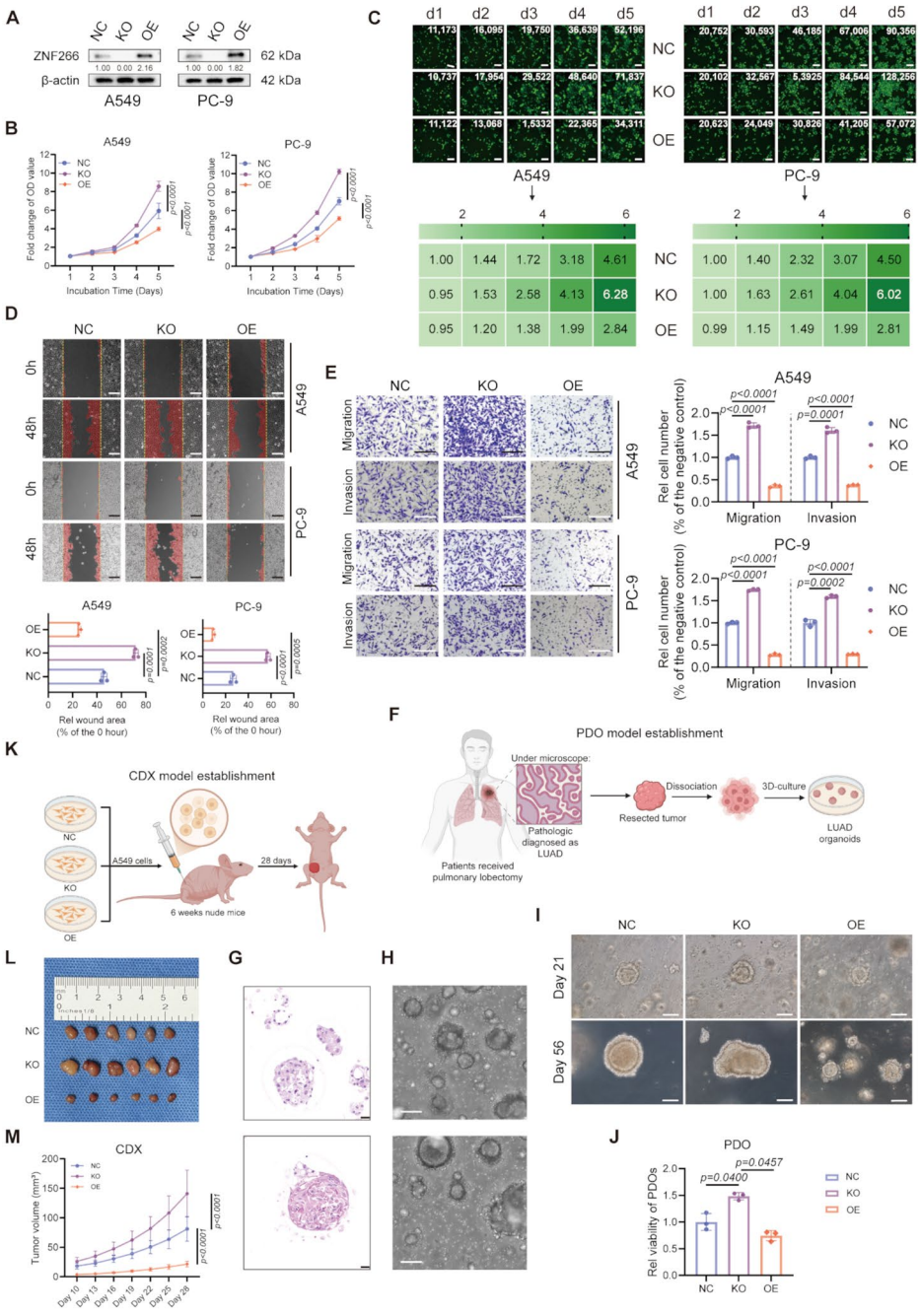

Fig. 2 ZNF266 inhibits the proliferation, migration, and invasion ability of LUAD. **(A)** Western blot analysis verifying the ZNF266 knockout and overexpression efficiency in A549 and PC-9 cells. **(B-C)** CCK8 assays ($n=6$ per group) **(B)** and high-content imaging analysis ($n=3$ per group) **(C)** show the effects of ZNF266 knockout and overexpression on cell proliferation in A549 and PC-9. Scale bars, 200 μm. **(D)** Wound-healing assays ($n=3$ per group) show the effects of ZNF266 knockout and overexpression on cell migration in A549 and PC-9. Scale bars, 200 μm. **(E)** Transwell assays ($n=3$ per group) show the effects of ZNF266 knockout and overexpression on cell migration and invasion in A549 and PC-9. Scale bars, 200 μm. **(F-H)** Establishment **(F)**, HE staining images **(G)**, and morphology **(H)** of LUAD patient-derived organoids (PDOs). Scale bars, 100–20 μm. **(I-J)** Representative brightfield images **(I)** and luminescence measurement ($n=3$ per group) **(J)** of PDOs in different groups. PDOs were transfected with lentiviruses to knockout or overexpress ZNF266. P values by one-way ANOVA. Partial $\eta^2=0.92$. KO vs. NC 95% CI of diff. = (0.22 to 0.73), OE vs. NC 95%CI of diff. = (-0.52 to -0.01). Scale bars, 100 μm. **(L-M)** Tumor images **(L)** and growth curves **(M)** of each group ($n=6$). P values by two-way ANOVA. Partial $\eta^2=0.51$. KO vs. NC 95% CI of diff. = (20.84 to 34.95), OE vs. NC 95%CI of diff. = (-39.95 to -25.85)

and molecular characteristics of the primary LUAD tissues were accurately recapitulated in the LUAD PDOs (Fig. 2G and H). We examined the morphology and measured the ATPase activity of PDOs (Fig. 2I and J), and discovered that the level of ZNF266 expression impacts the vitality and growth of organoids, aligning with what we've observed in cellular assays.

To verify the findings in vivo, we conducted cell line-derived xenograft (CDX) tumor formation assays in nude mice ($n = 6$ for each group) (Fig. 2K). A549 cells from different groups were injected subcutaneously into nude mice. It was observed that ZNF266 overexpression significantly inhibited tumor formation, whereas ZNF266 deletion promoted tumor progression (Fig. 2L and M). Our results confirmed that ZNF266 expression level impacts the hallmarks of LUAD both in vitro and in vivo.

ZNF266 represses CA9's transcription by binding to its promotor

To determine potential downstream targets of ZNF266, RNA-seq was conducted in ZNF266-NC and ZNF266-OE cells respectively (Fig. 3A) and differentially expressed genes (DEGs) were displayed (Fig. 3B). The results revealed that CA9 stood out as the most significant gene among the five with notably altered expression levels in both A549 and PC-9 cells (Fig. 3C), suggesting that CA9 might be a target molecule of ZNF266. Additional verification of the effect of ZNF266 on CA9 expression was conducted using qRT-PCR and Western blot analysis. The results demonstrated that overexpression of ZNF266 led to a decrease in CA9 levels, whereas ZNF266 knockout resulted in the upregulation of CA9 (Fig. S2B and 3D).

We speculate that ZNF266 transcriptionally suppressed CA9 by binding to its promotor. Utilizing the genome-wide chromatin immunoprecipitation sequencing (ChIP-seq) data published by the ENCODE project, we found three very strong ZNF266-binding peaks in the CA9 promotor region (between − 1,000 and + 500 bp to the transcription start site [TSS]) (Fig. 3E-G). To confirm the binding of ZNF266 to the CA9 promoter in LUAD cell lines, ChIP-qPCR assays were conducted, revealing significant recruitment of ZNF266 to the CA9 promoter region (Fig. 3H). Consistently, DNA pull-down assays demonstrated that oligonucleotides spanning the wild-type CA9 promotor region, but not the mutant, exhibited significant affinity for ZNF266 (Fig. 3I). These results confirm that ZNF266 can directly bind to the CA9 promotor.

Subsequently, the CA9 promoter sequences were cloned into the pGL4-luciferase reporter vector to assess the transcriptional functionality of ZNF266 binding. As a negative control, we predicted and modified all the sites where ZNF266 most likely binds (threshold ≥ 0.8) using the consensus motifs on the JASPAR website. It was observed that the expression of ZNF266 significantly reduced the activity of the luciferase reporter containing the wild-type CA9 promoter sequence (Fig. 3J). In contrast, the introduction of mutations to the CA9 promoter region attenuated this change. These observations suggest that ZNF266 directly regulates CA9 transcription by binding to its promotor region.

In addition, a negative correlation was observed between ZNF266 and CA9 expression in resected tissue from LUAD patients (Fig. 3K and L) and in immunofluorescence analysis of CDX tumors (Fig. 3M), also indicating their negative regulation.

ZNF266 restrains the mTOR signaling pathway by decreasing intracellular pH

Data from the TCGA and GTEx databases showed that CA9 expression was elevated in LUAD (Fig. 4A), which indicated a poor clinical prognosis for patients (Fig. 4B). CA9 catalyzes the reversible hydration of CO_2 at the exofacial site of the plasma membrane, making CA9 centrally in the regulation of intracellular pH (pHi) and extracellular pH (pHe). CA9 maintains a steep outward-directed CO_2 gradient across the plasma membrane, facilitating CO_2 excretion, which subsequently leads to extracellular acidification and a more alkaline pHi [17–19]. Morphology and flow cytometry with BCECF-AM probes demonstrated a decreased pHi in the ZNF266-OE LUAD cells and an increased pHi in the ZNF266-KO LUAD cells. This finding is consistent with ZNF266's CA9-suppressing role. (Figure 4C and D).

It is noteworthy that Kyoto Encyclopedia of Genes and Genomes (KEGG) analyses indicated that the DEGs between ZNF266-NC and ZNF266-OE were predominantly enriched in the mTOR signaling pathway in both A549 and PC-9 (Fig. 4E and F), suggesting a regulatory role for ZNF266 in the mTOR signaling pathway in LUAD. Therefore, we detected the phosphorylation level of mTOR and S6K, the classic downstream of mTORC1, and found that ZNF266 overexpression reduced the phosphorylation of both mTOR and S6K and vice versa, supportively (Fig. 4G).

Furthermore, prestigious research has reported the impact of pHi on the mTOR signaling pathway, revealing that a reduction in pHi inhibits the activation of mTORC1, a key complex within the mTOR signaling pathway [20, 21], while dysregulated mTORC1 contributes causally to cancer development and progression [22–24]. We adjusted the pH of the LUAD cell culture medium for 48 h by adding HCl or NaOH (pH = 6.5, 7.0, and 7.5) and noticed the changed pHi (Fig. 4H), and the subsequent Western blot analysis confirmed that the mTOR signaling pathway was regulated by pHi in LUAD cells (Fig. 4I).

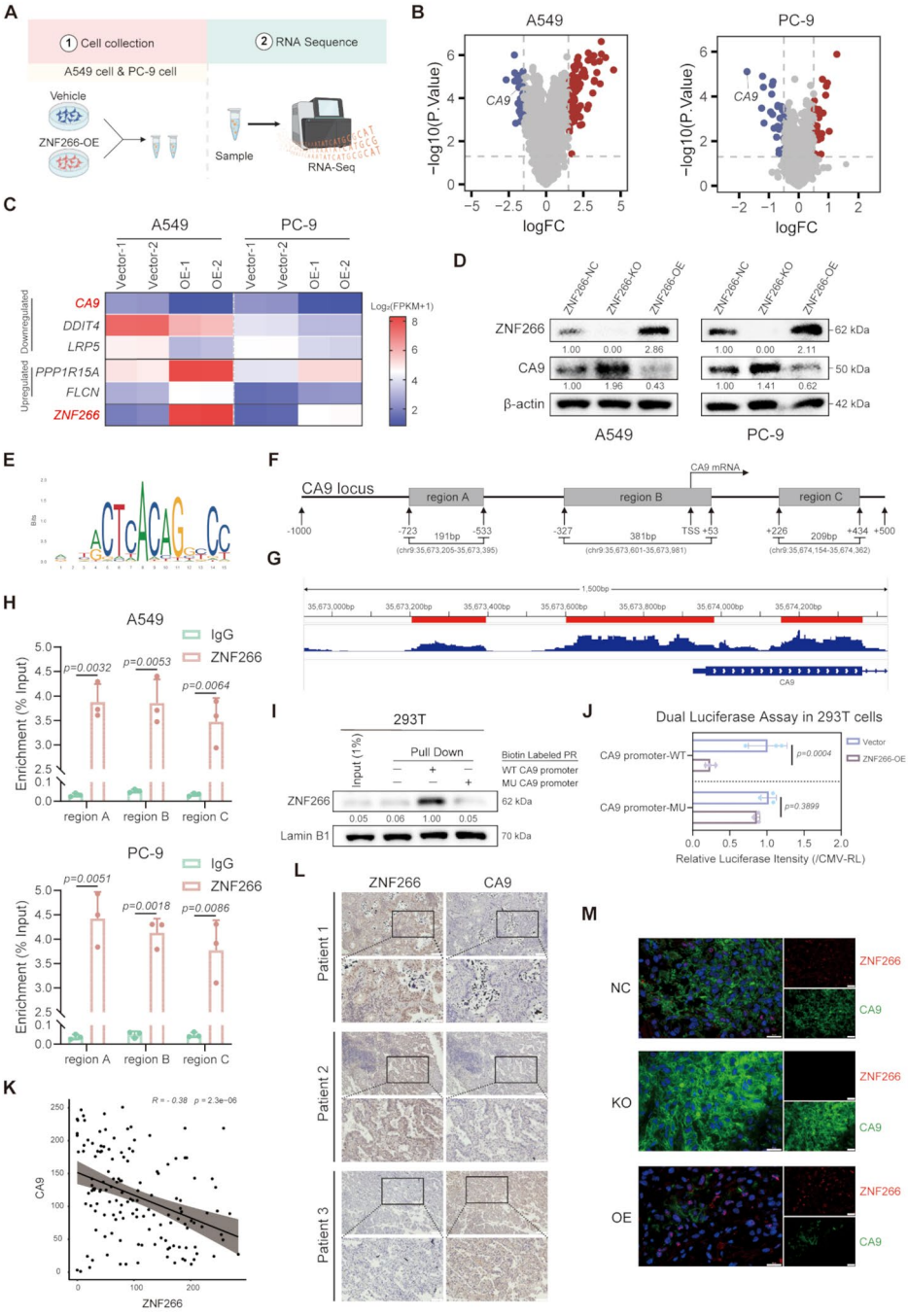

Fig. 3 ZNF266 represses CA9's transcription by binding to its promotor. **(A)** Schematic diagram of RNA sequencing in A549 and PC-9 cells stably overexpressing ZNF266. **(B-C)** Volcano plot **(B)** and heatmap **(C)** exhibit differentially expressed genes between ZNF266-OE and NC groups in A549 and PC-9. CA9 stands out. **(D)** Western blot analysis confirms regulated CA9 expression after ZNF266 knockout and overexpression. **(E)** Characteristic sequences predicted by JASPAR for transcriptional binding sites of ZNF266. **(F-G)** Genome-wide data and ChIP-seq results from the ENCODE project show the solid ZNF266-binding peak in the promoter region to the TSS of CA9. **(H)** ChIP-qPCR assays ($n = 3$ per group) depicting the enrichments of ZNF266 binding in A549 and PC-9. **(I)** Western blot analysis of exogenous ZNF266 and Lamin B1 (control) protein pulled down by biotin-labeled oligonucleotides containing the wild-type or mutant CA9 promoter. **(J)** Dual luciferase activity assays ($n = 3$ per group) to analyze the fluorescence intensity of ZNF266-OE and NC with or without mutations in the CA9 promoter region. **(K-L)** Pearson correlation analysis between ZNF266 and CA9 expression in LUAD patient samples **(K)** and representative IHC images **(L)**. Scale bars, 200–100 μm. **(M)** Representative multiplex IHC (mIHC) images of CDX tumors. Scale bars, 20 μm

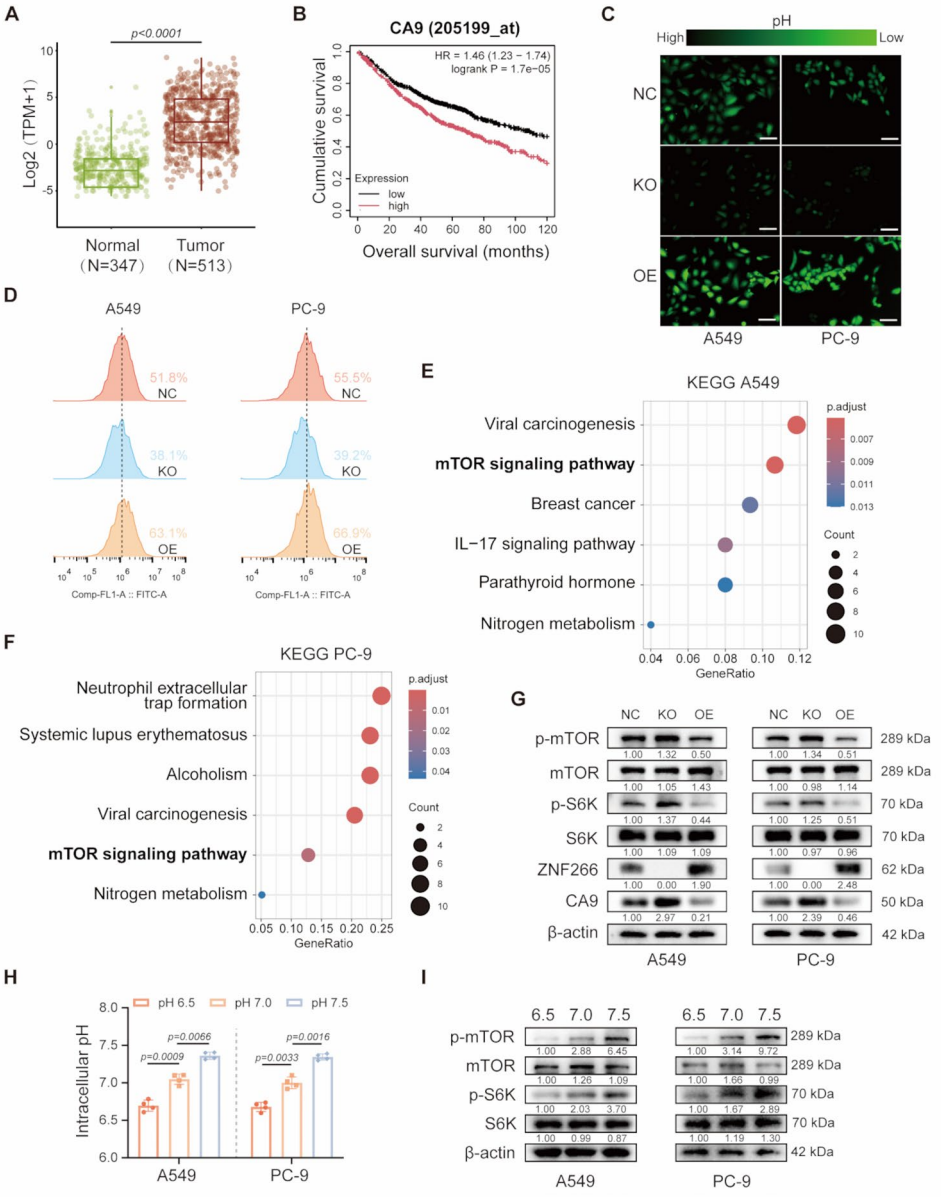

Fig. 4 ZNF266 restrains the mTOR signaling pathway via intracellular pH. **(A)** CA9 expression levels in normal and tumor samples from the TCGA-LUAD and GTEx databases (normal group = 347, tumor group = 513). **(B)** Kaplan–Meier analysis of overall survival comparing the high and low expression of CA9 in LUAD patients in the Kaplan–Meier plotter database. **(C-D)** Morphology **(C)** and flow cytometry **(D)** with BCECF-AM probes exhibit the effects of ZNF266 knockout or overexpression on pHi in A549 and PC-9. Scale bars, 100 μm. **(E-F)** KEGG enrichment analysis of differentially expressed genes in our RNA-seq data. **(G)** Western blot analysis of the effects of ZNF266 knockout and overexpression on phosphorylation of the mTOR signaling pathway in A549 and PC-9 cells. **(H)** Measurement of pHi ($n = 4$ per group) in A549 and PC-9 cells incubated with different pH for 48 h. **(I)** Western blot analysis confirms the effects of different pHi on phosphorylation of the mTOR signaling pathway in A549 and PC-9 cells incubated in medium with indicating pH for 48 h

Based on these findings, we hypothesized that ZNF266 might regulate the activation of the mTOR pathway through CA9-mediated pHi alteration, thereby influencing the malignant phenotypes of cancer.

CA9 expression abrogates the effect of ZNF266 on malignant phenotypes of LUAD

To validate our hypothesis, CA9 expression was restored in ZNF266-OE and NC LUAD cells (Fig. S2C, S2D, and 5C). We observed that CA9 restoration eliminated the difference between ZNF266-OE and NC in terms of the pHi and the phosphorylation level of the mTOR pathway (Fig. 5A and B). Subsequently, CCK8 assays and

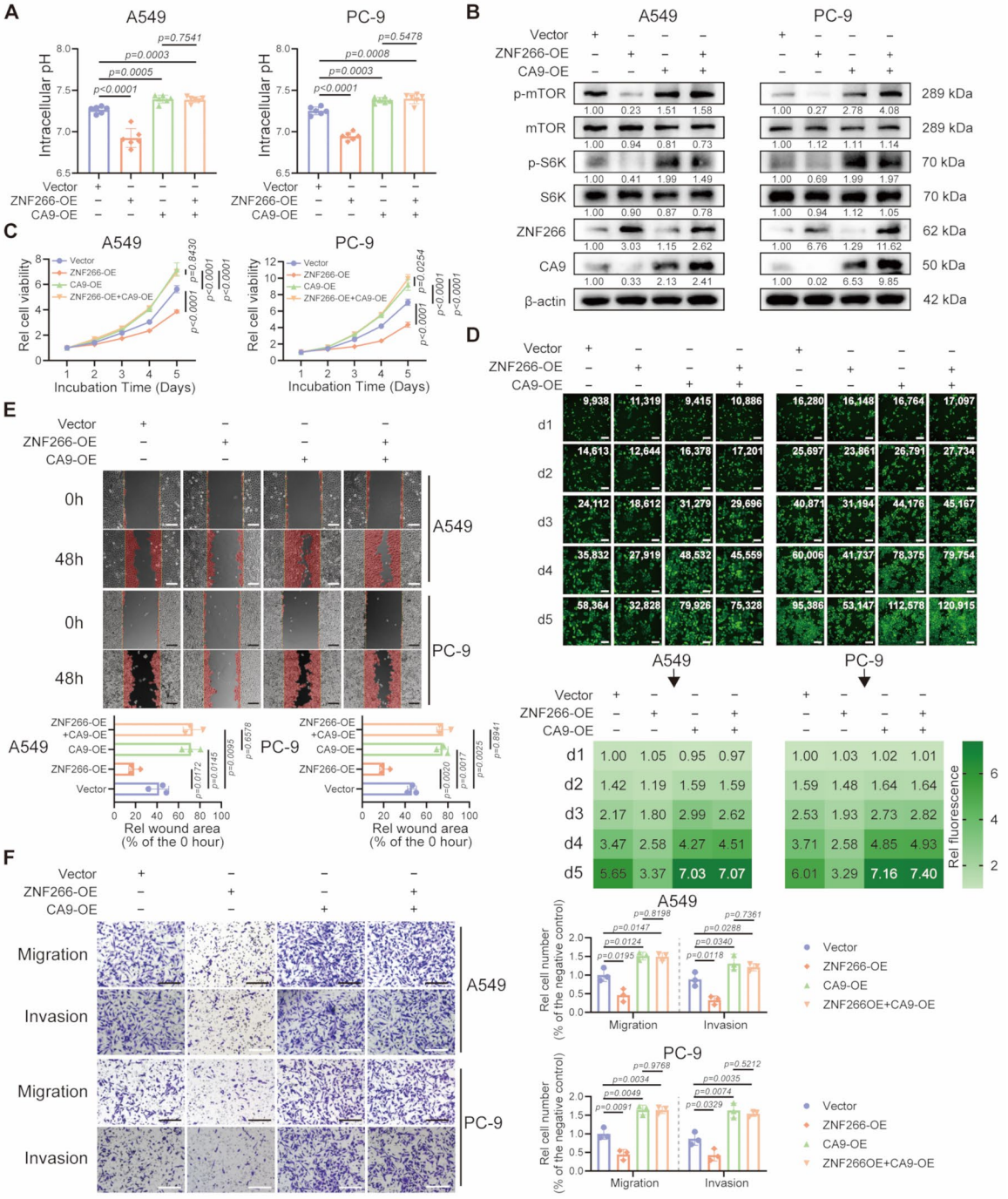

Fig. 5 CA9 expression abrogates the effect of ZNF266 on malignant phenotypes of LUAD cells. **(A)** Measurement of pHi ($n=6$ per group) in A549 and PC-9 transfected with ZNF266-NC, ZNF266-OE, CA9-OE, and ZNF266-OE + CA9-OE lentiviruses. **(B)** Western blot analysis of ZNF266 expression level, CA9 expression level, and phosphorylation of the mTOR signaling pathway in A549 and PC-9 cells of different groups. **(C-D)** CCK8 assays ($n=6$ per group) **(C)** and high-content imaging analysis ($n=3$ per group) **(D)** show the effects of CA9 restoration on cell proliferation inhibited by ZNF266 in A549 and PC-9 cells. Scale bars, 200 μm. **(E)** Wound-healing assays ($n=3$ per group) show the effects of CA9 restoration on cell migration inhibited by ZNF266 in A549 and PC-9 cells. Scale bars, 200 μm. **(F)** Transwell assays ($n=3$ per group) show the effects of CA9 restoration on cell migration and invasion inhibited by ZNF266 in A549 and PC-9. Scale bars, 200 μm

high-content imaging analysis showed that cells with restored CA9 expression exhibited similar proliferation capacities, regardless of the expression level of ZNF266 (Fig. 5C and D). Wound healing and transwell assays indicated that the overexpression of CA9 significantly mitigated the inhibitory effects of ZNF266 on migration and invasion in LUAD cells (Fig. 5E and F). Similar findings were observed in PDOs, where both morphology and the ATPase activity were consistent with these results (Fig. 6A and B). Additionally, immunohistochemistry analysis showed that the differences in Ki-67 levels were eliminated by CA9 restoration (Fig. 6C).

Subcutaneous tumor formation assays were performed to verify the results obtained above in vivo. In alignment with the in vitro results, tumor formation was significantly boosted in nude mice injected with CA9-overexpressing cells compared to the ZNF266-OE and NC groups. More importantly, irrespective of ZNF266 expression levels, tumorigenesis following subcutaneous injection of CA9-overexpressing cells in nude mice yielded similar results (Fig. 6D and E).

Collectively, the results above suggested that ZNF266 regulates the activation of the mTOR pathway via CA9-mediated pHi alteration, ultimately affecting the malignant phenotypes of LUAD.

Therapeutic potential of AAV-ZNF266 in LUAD

To assess the therapeutic potential of ZNF266 in LUAD, we investigated its efficacy in preclinical PDX models. Following confirmation of AAV-ZNF266 biosafety (Fig. S3A-3Q), two PDX models (PDX-1 and PDX-2) were generated from treatment naïve LUAD specimens. Third-generation xenografts received peritumoral AVV-ZNF266 delivery (Fig. 6F), which significantly suppressed tumor growth over an 18-day observation window (Fig. 6G and H), recapitulating the inhibitory effects observed in CDX models. Following euthanasia, tumors from NSG mice were dissected for gravimetric analysis and immunohistochemistry staining. ZNF266-overexpressing tumors exhibited marked downregulation of CA9 protein levels compared to controls, alongside diminished Ki-67 positivity (Fig. 6I), indicative of impaired proliferation capacity. These findings positioned ZNF266 restoration as a promising translational strategy for LUAD (Fig. 6J).

Discussion

LUAD is characterized by prevalent and highly aggressive malignant phenotypes with a poor prognosis. It displays the fundamental traits of malignancies, including the ability to sustain chronic proliferation, bypass potent inhibitory mechanisms that regulate cellular growth, and facilitate invasion and metastasis. There is currently an urgent need to identify new therapeutic targets for LUAD and to elucidate the mechanisms underlying them [25].

TFs serve as pivotal regulators of gene expression across all cancer hallmarks, influencing processes such as cellular proliferation and metastatic dissemination. Historically regarded as undruggable due to structural disorganization and the lack of defined small-molecule binding sites, recent advancements in structural elucidation, fundamental biological understanding, and ligand design methodologies have facilitated the discovery of several promising therapeutic agents targeting TFs, such as RGT-61,159 and TTI-101 [7, 8]. Approximately 1,600 TFs are estimated to exist in the human genome, yet the functions of the majority of these factors and their therapeutic potential in cancer remain largely unexplored.

This study delved into the pivotal role of ZNF266 in LUAD. By leveraging a large cohort of nearly three thousand samples from public databases alongside our specimens, we present the initial comprehensive analysis of the clinical relevance of ZNF266 in LUAD. Our study provides the first evidence that ZNF266 mediates an inhibitory effect via a mechanism that encompasses the suppression of CA9 transcription and consequent inhibition of the mTOR pathway. Manipulation of ZNF266 expression levels in organoid models and overexpression of ZNF266 using adeno-associated virus in PDX models has led to significant findings.

In mammalian cells, zinc finger proteins (ZNFs) constitute the most extensive family of transcription factors. Dysregulation of ZNF expression is observed in various tumor types, implying potential functions as oncogenes or tumor suppressors [26, 27]. ZNF266 is a member of the zinc finger protein family and comprises many zinc-finger motifs arranged in tandem [28]. These zinc fingers serve as binding domains for proteins or nucleic acids and may participate in diverse functions, notably transcription regulation [5, 29, 30]. It has been reported by Jinhui Zhang et al. that ZNF266 may serve as a promising candidate gene with a causal association with the survival risk of cervical cancer [31]. Nonetheless, the mechanisms and regulatory functions of ZNF266 remain elusive and may vary across cancer types, necessitating further exploration.

Our research suggests that ZNF266-CA9-pHi-mTOR axis modulates the progression of LUAD. Solid tumors frequently exhibit acidic regions due to hypoxia. The acidic microenvironment poses a selective pressure on cancer cells, and CA9 plays a pivotal role in enabling cancer cell adaptation by converting high CO_2 levels into H^+ and HCO_3^- [32]. These adaptations facilitate the maintenance of a slightly alkaline pHi in cancer cells [19, 33]. The mammalian target of rapamycin, discovered 30 years ago, is a highly conversed serine/threonine protein kinase that plays a central role in regulating cell growth and

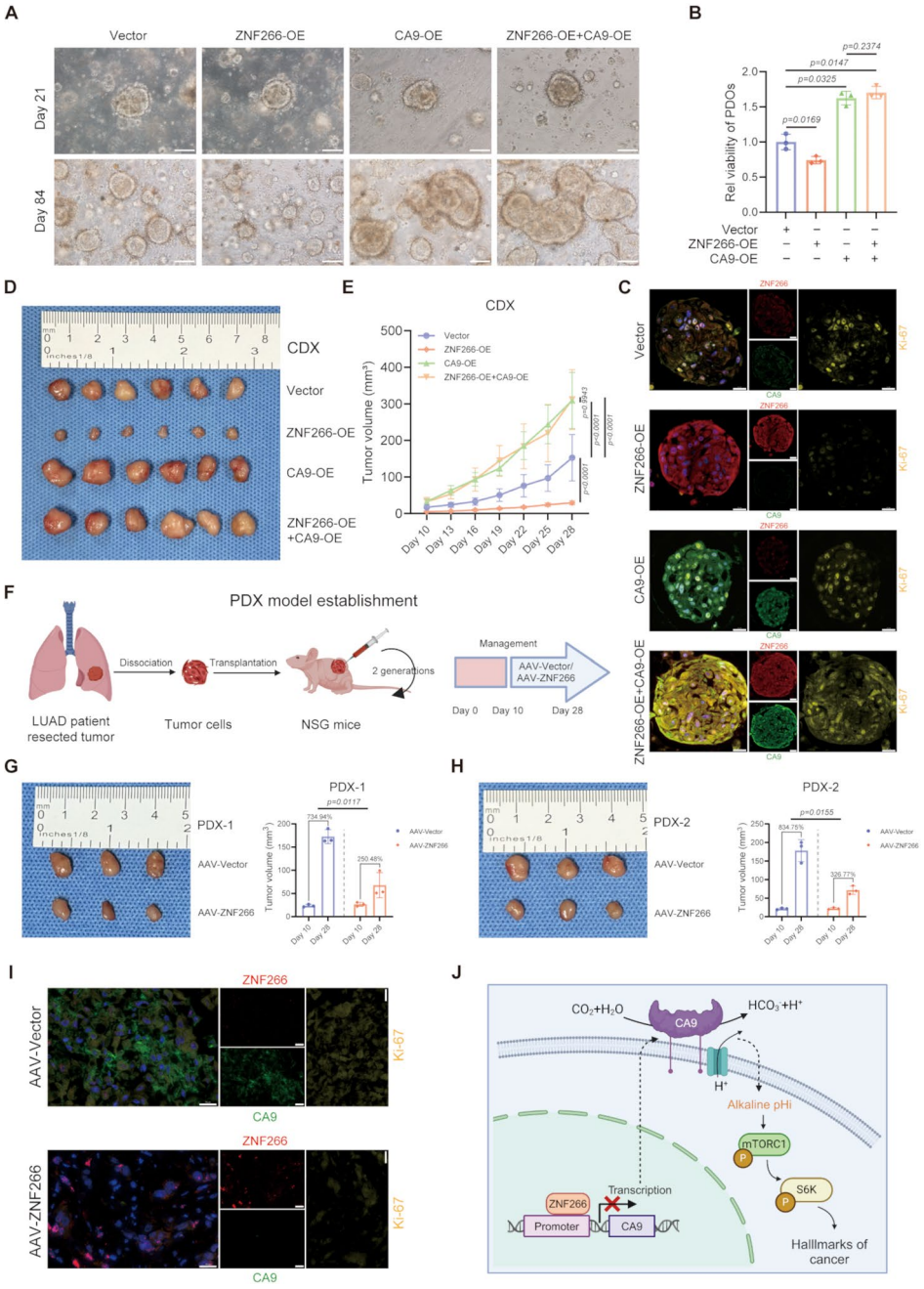

Fig. 6 ZNF266 inhibits LUAD progression via regulating CA9 expression in PDOs and xenograft models. **(A-C)** Representative brightfield images **(A)**, mIHC images **(B)**, and luminescence measurement ($n = 3$ per group) **(C)** of PDOs in different groups. PDOs were transfected with lentiviruses to overexpress ZNF266 or CA9. Scale bars, 100 μm–20 μm. P values by one-way ANOVA. Partial $\eta^2 = 0.97$. ZNF266-OE vs. Vector 95% CI of diff. = (-0.51 to -0.01), CA9-OE vs. Vector 95%CI of diff. = (0.37 to 0.88), ZNF266-OE + CA9-OE vs. Vector 95% CI of diff. = (0.45 to 0.96), CA9-OE vs. ZNF266-OE + CA9-OE 95% CI of diff. = (-0.33 to 0.17). **(D-E)** Tumor images **(D)** and growth curves **(E)** of CDX models ($n = 6$ per group). P values by two-way ANOVA. Partial $\eta^2 = 0.31$. ZNF266-OE vs. Vector 95% CI of diff. = (-56.31 to -3.48), CA9-OE vs. Vector 95%CI of diff. = (53.73 to 113.53), ZNF266-OE + CA9-OE vs. Vector 95% CI of diff. = (66.80 to 126.60), CA9-OE vs. ZNF266-OE + CA9-OE 95% CI of diff. = (-42.97 to 16.83). **(F)** Schematic representation of establishment of two patient-derived xenograft (PDX) models and following adeno-associated virus (AAV) treatment. **(G-H)** Tumor images and volumes ($n = 3$ per group) of PDX-1 **(G)** and PDX-2 **(H)** injecting AAV-ZNF266 or AAV-Vector. **(G)** P values by Student's t-test. Cohen's d = 4.75. AAV-ZNF266 vs. ZNF266-Vector 95% CI of diff. = (54.77 to 154.60). **(H)** P values by Student's t-test. Cohen's d = 4.76. AAV-ZNF266 vs. ZNF266-Vector 95% CI of diff. = (55.89 to 157.67). **(I)** Representative mIHC images of PDX tumors. Scale bars, 20 μm. **(J)** Model for ZNF266 inhibiting LUAD progression by regulating CA9-mediated intracellular pH

metabolism [34, 35]. Dysregulation of mTOR has been implicated in several major diseases [36], including many types of cancers [22, 37, 38]. Zandra E. Walton et al. have reported that acidic intracellular conditions promote the redistribution of lysosomes to the cellular periphery, thereby separating mTORC1 from its perinuclear activator RHEB and disrupting the circadian clock [20, 39]. This pHi-mTOR axis has not been previously reported in the context of tumors, and we validated the existence of this axis in LUAD for the first time and extrapolated the conclusion to the malignant phenotype of tumors. Cellular signaling architectures function as highly integrated, pleiotropic systems transcending simplistic linear cascades. Although our dissection of ZNF266 interactome dynamics may not exhaustively map all tertiary effectors within this multidimensional network, we establish through mechanistic and functional validation a novel tumor-suppressive axis (ZNF266-CA9-pHi-mTOR) essential for maintaining LUAD oncogene addiction.

While elucidating this downstream circuitry, upstream modulators governing ZNF266's oncogenic subversion in LUAD remain unresolved, which is a limitation tied to the systems biology challenge of revealing transcription factor regulation in vivo. This limitation presents opportunities for leveraging multi-omics approaches to delineate mechanisms that may drive ZNF266 dysregulation through chromatin topology remodeling or non-coding RNA-mediated control [40], which we hope future studies will address.

Modulation of ZNF266 expression in organoid models, along with increased ZNF266 expression using AAV vectors in PDX models derived from patients, has yielded notable results. During long-term in vitro culture, the PDOs maintained the genetic alterations present in the original tumors, allowing for the investigation of the mechanisms underlying tumor evolution [41]. AAV-based gene delivery vectors have been employed in numerous clinical trials for gene therapy and have demonstrated a robust safety profile as well as efficacious treatment of monogenic disorders [42]. While the off-target effects and immune responses linked to AAV-mediated gene therapy remain incompletely elucidated [43], accumulating preclinical and clinical evidence highlights its promising therapeutic potential as a targeted intervention in oncology [44–46]. PDX models, in which tumor tissues obtained from patients are engrafted into immunocompromised or humanized mice, demonstrate enhanced accuracy in recapitulating cancer characteristics, such as the spatial organization and intratumoral heterogeneity of the tumor [47]. Application of AAV to PDX models enables more precise simulation of the clinical outcomes of ZNF266 therapy. However, PDX models utilized NSG mice, which inherently lack T cells, B cells, and NK cells, thereby precluding direct evaluation of AAV-ZNF266's effects on immune cell infiltration. To resolve this limitation and rigorously dissect the interplay between AAV-ZNF266 and adaptive immunity, future studies will assess its therapeutic efficacy and potential synergies with immunotherapeutic agents in syngeneic or immunocompetent murine models.

Conclusion

Our study identified ZNF266 as a prognostic biomarker and demonstrated that ZNF266 inhibits LUAD progression in a pH-dependent manner via modulating CA9 expression. These findings revealed that ZNF266 might be a prospective target for LUAD treatment.

Abbreviations

LUAD	Lung adenocarcinoma
ZNF266	Zinc Finger Protein 266
AAV	Adeno-associated virus
mTOR	mammalian target of rapamycin
NSCLC	Non-small cell lung cancer
TF	Transcription factor
CA9	Carbonic anhydrase IX
TCGA	The Cancer Genome Atlas Program
GTEx	Genotype-Tissue Expression
RNA-seq	RNA sequencing
PCR	Polymerase chain reaction
qRT-PCR	quantitative real-time PCR
IHC	Immunohistochemistry
OS	Overall survival
PDOs	Patient-derived organoids
NC	Negative control
OE	Overexpressing-after-knockout
KO	Knockout
CDX	Cell line-derived xenograft
DEGs	Differentially expressed genes
ChIP-seq	Chromatin immunoprecipitation sequencing
TSS	Transcription start site
pHi	intracellular pH
pHe	extracellular pH
KEGG	Kyoto Encyclopedia of Genes and Genomes
PDX	Patient-derived tumor xenograft
CDS	Coding sequence
NSG	NOD SCID gamma
ZNF	Zinc finger protein

Supplementary Information

The online version contains supplementary material available at https://doi.org/10.1186/s12931-025-03278-7.

Supplementary Material 1

Supplementary Material 2

Acknowledgements

Not applicable.

Author contributions

C.Z., G.B., D.G., and S.R. conceived the project and designed the work. H.S. and B.P. performed the bioinformatic analysis. S.R., J.Z., and G.S. performed most of the experiments. J.L., Y.B., and H.L. contributed to cell culture and ChIP assays. S.R., J.Z., and G.S. generated organoids. G.S., S.R., and B.P. performed IHC staining and animal experiments. G.Z., H.Y., and X.H. analysed the data. G.B. and D.G. supervised statistical analysis. S.R. worte the paper. D.G., C.Z., G.S., and G.B. reviewed and revised the manuscript. All authors discussed and approved the final manuscript.

Funding
This work was supported by grants from The National Natural Science Foundation of China (No. 82403100, 82473184, 82472910), the Natural Science Foundation of Shanghai (No. 24ZR1409900), and the China Postdoctoral Science Foundation (No. 2024M760555).

Data availability
No datasets were generated or analysed during the current study.

Declarations

Ethics approval and consent to participate
This study strictly adhered to the ethical guidelines established in the Declaration of Helsinki and received approval from the Research Ethics Committee of Zhongshan Hospital, Fudan University (approval number: B2022-180R).

Consent for publication
Informed consent was obtained from all individual participants included in the study.

Competing interests
The authors declare no competing interests.

Clinical trial number
Not applicable.

Author details
[1]Department of Thoracic Surgery, Zhongshan Hospital, Fudan University, Shanghai 200032, China
[2]Department of Thoracic Surgery, Shanghai Geriatric Medical Center, Fudan University, Shanghai 201104, China

Received: 11 January 2025 / Accepted: 15 May 2025
Published online: 19 May 2025

References

1. Bray F, et al. Global cancer statistics 2022: GLOBOCAN estimates of incidence and mortality worldwide for 36 cancers in 185 countries. CA Cancer J Clin. 2024;74(3):229–63.
2. Thai AA, et al. Lung cancer. Lancet. 2021;398(10299):535–54.
3. Allemani C, et al. Global surveillance of trends in cancer survival 2000-14 (CONCORD-3): analysis of individual records for 37 513 025 patients diagnosed with one of 18 cancers from 322 population-based registries in 71 countries. Lancet. 2018;391(10125):1023–75.
4. Miller KD, et al. Cancer treatment and survivorship statistics, 2022. CA Cancer J Clin. 2022;72(5):409–36.
5. Lambert SA, et al. The human transcription factors. Cell. 2018;172(4):650–65.
6. Hanahan D. Hallmarks of cancer: new dimensions. Cancer Discov. 2022;12(1):31–46.
7. Xi S, et al. Effect of RGT-61159 on Inhibition of oncogene c-MYB synthesis and tumor growth Inhibition in a broad range of ACC PDX models, at well tolerated doses in rodents and non-human primates. J Clin Oncol. 2024;42(16suppl):6107–6107.
8. Tsimberidou AM, et al. Phase 1 trial evaluating TTI-101, a first-in-class, orally bioavailable, small molecule, inhibitor of STAT3, in patients with advanced solid tumors. J Clin Oncol. 2023;41(16suppl):3018–3018.
9. Niu H, et al. Knockdown of SMAD3 inhibits the growth and enhances the radiosensitivity of lung adenocarcinoma via p21 in vitro and in vivo. Int J Biol Sci. 2020;16(6):1010–22.
10. Zhang H, et al. AGRN promotes lung adenocarcinoma progression by activating Notch signaling pathway and acts as a therapeutic target. Pharmacol Res. 2023;194:106819.
11. Shan G, et al. Targeting ALDH2 to augment platinum-based chemosensitivity through ferroptosis in lung adenocarcinoma. Free Radic Biol Med. 2024;224:310–24.
12. Bian Y, et al. Targeting ALDH1A1 to enhance the efficacy of KRAS-targeted therapy through ferroptosis. Redox Biol. 2024;77:103361.
13. Bi G, et al. Polyamine-mediated ferroptosis amplification acts as a targetable vulnerability in cancer. Nat Commun. 2024;15(1):2461.
14. Shan G, et al. Sarcosine sensitizes lung adenocarcinoma to chemotherapy by dual activation of ferroptosis via PDK4/PDHA1 signaling and NMDAR-mediated iron export. Exp Hematol Oncol. 2025;14(1):60.
15. Lin J, et al. A positive feedback loop between ZEB2 and ACSL4 regulates lipid metabolism to promote breast cancer metastasis. Elife. 2023;12:RP87510.
16. Li Y, et al. ZEB2 facilitates peritoneal metastasis by regulating the invasiveness and tumorigenesis of cancer stem-like cells in high-grade serous ovarian cancers. Oncogene. 2021;40(32):5131–41.
17. Becker HM. Carbonic anhydrase IX and acid transport in cancer. Br J Cancer. 2020;122(2):157–67.
18. Li Z, et al. Carbonic anhydrase 9 confers resistance to ferroptosis/apoptosis in malignant mesothelioma under hypoxia. Redox Biol. 2019;26:101297.
19. Queen A, et al. Carbonic anhydrase IX: A tumor acidification switch in heterogeneity and chemokine regulation. Semin Cancer Biol. 2022;86(Pt 3):899–913.
20. Walton ZE, et al. Acid suspends the circadian clock in hypoxia through Inhibition of mTOR. Cell. 2018;174(1):72–e8732.
21. Goul C, Peruzzo R, Zoncu R. The molecular basis of nutrient sensing and signalling by mTORC1 in metabolism regulation and disease. Nat Rev Mol Cell Biol. 2023;24(12):857–75.
22. Chiang GG, Abraham RT. Targeting the mTOR signaling network in cancer. Trends Mol Med. 2007;13(10):433–42.
23. Szwed A, Kim E, Jacinto E. Regulation and metabolic functions of mTORC1 and mTORC2. Physiol Rev. 2021;101(3):1371–426.
24. Kim J, Guan KL. mTOR as a central hub of nutrient signalling and cell growth. Nat Cell Biol. 2019;21(1):63–71.
25. Liang J, et al. MAFF confers vulnerability to cisplatin-based and ionizing radiation treatments by modulating ferroptosis and cell cycle progression in lung adenocarcinoma. Drug Resist Updat. 2024;73:101057.
26. Zhao J, et al. The role of zinc finger proteins in malignant tumors. Faseb J. 2023;37(9):e23157.
27. Liu S, et al. Zinc finger proteins in the war on gastric cancer: molecular mechanism and clinical potential. Cells. 2023;12(9):1314.
28. Peng H, Du ZW, Zhang JW. Identification and characterization of a novel zinc finger protein (HZF1) gene and its function in erythroid and megakaryocytic differentiation of K562 cells. Leukemia. 2006;20(6):1109–16.
29. Brayer KJ, Segal DJ. Keep your fingers off my DNA: protein-protein interactions mediated by C2H2 zinc finger domains. Cell Biochem Biophys. 2008;50(3):111–31.
30. Campagne S, et al. Structural determinants of specific DNA-recognition by the THAP zinc finger. Nucleic Acids Res. 2010;38(10):3466–76.
31. Zhang J, et al. Leveraging methylation alterations to discover potential causal genes associated with the survival risk of cervical Cancer in TCGA through a Two-Stage inference approach. Front Genet. 2021;12:667877.
32. Pastorekova S, Gillies RJ. The role of carbonic anhydrase IX in cancer development: links to hypoxia, acidosis, and beyond. Cancer Metastasis Rev. 2019;38(1–2):65–77.
33. Aldera AP, Govender D. Carbonic anhydrase IX: a regulator of pH and participant in carcinogenesis. J Clin Pathol. 2021;74:350–6.
34. Webb BA, et al. Dysregulated pH: a perfect storm for cancer progression. Nat Rev Cancer. 2011;11(9):671–7.
35. Bi G, et al. Retinol saturase mediates retinoid metabolism to impair a ferroptosis defense system in Cancer cells. Cancer Res. 2023;83(14):2387–404.
36. Liao G, et al. Nestin drives allergen-induced airway smooth muscle hyperplasia and airway remodeling. Allergy. 2024;79(3):744–6.
37. Battaglioni S, et al. mTOR substrate phosphorylation in growth control. Cell. 2022;185(11):1814–36.
38. Wang C, et al. Multi-omics analyses reveal biological and clinical insights in recurrent stage I non-small cell lung cancer. Nat Commun. 2025;16(1):1477.
39. Yang H, et al. Mechanisms of mTORC1 activation by RHEB and Inhibition by PRAS40. Nature. 2017;552(7685):368–73.
40. Wang C, et al. Characterization of distinct circular RNA signatures in solid tumors. Mol Cancer. 2022;21(1):63.
41. Kim M, et al. Patient-derived lung cancer organoids as in vitro cancer models for therapeutic screening. Nat Commun. 2019;10(1):3991.
42. Santiago-Ortiz JL, Schaffer DV. Adeno-associated virus (AAV) vectors in cancer gene therapy. J Control Release. 2016;240:287–301.
43. Dhungel BP, et al. Understanding AAV vector immunogenicity: from particle to patient. Theranostics. 2024;14(3):1260–88.

44. Liang J, et al. Transcription factor ZNF263 enhances EGFR-targeted therapeutic response and reduces residual disease in lung adenocarcinoma. Cell Rep. 2024;43(2):113771.
45. Platt RJ, et al. CRISPR-Cas9 knockin mice for genome editing and cancer modeling. Cell. 2014;159(2):440–55.
46. Ramachandran M, et al. Tailoring vascular phenotype through AAV therapy promotes anti-tumor immunity in glioma. Cancer Cell. 2023;41(6):1134–e115110.
47. Liu Y, et al. Patient-derived xenograft models in cancer therapy: technologies and applications. Signal Transduct Target Ther. 2023;8(1):160.

Publisher's note